The Astrophysical Journal, 742:19 (14pp), 2011 November 20 doi:10.1088/0004-637X/742/1/19

A GRAND DESIGN FOR GALAXY CLUSTERS: CONNECTIONS AND PREDICTIONS

A. Cavaliere[1,2], A. Lapi[1,3], and R. Fusco-Femiano[4]
[1] Dipartimento di Fisica, Universitá degli Studi di Roma "Tor Vergata," Via della Ricerca Scientifica 1, I-00133 Roma, Italy
[2] INAF, Osservatorio Astronomico di Roma, via Frascati 33, I-00040 Monteporzio, Italy
[3] SISSA, Via Bonomea 265, I-34136 Trieste, Italy
[4] INAF-IASF, Via Fosso del Cavaliere, I-00133 Roma, Italy
Received 2011 April 6; accepted 2011 October 7; published 2011 November 2

ABSTRACT

We analyze with our entropy-based Supermodel a library of 12 galaxy clusters featuring extended X-ray observations of their intracluster plasma (ICP). The few intrinsic parameters of the model—basically, the central level and the outer slope of the entropy profile—enable us to uniformly derive not only robust snapshots of the ICP thermal state, but also the "concentration" parameter marking the age of the host dark matter (DM) halo. We test these profiles for consistency with numerical simulations and observations. We find the central and the outer entropy correlate, so that these clusters split into two main classes defined on the basis of low (LE) or high entropy (HE) conditions prevailing *throughout* the ICP. We also find inverse *correlations* between the central/outer entropy and the halo concentration. We interpret these in terms of mapping the ICP progress on timescales around 5 Gyr toward higher concentrations, under the drive of the DM halo development. The progress proceeds from HE clusters to LE clusters, toward states of deeper entropy erosion by radiative cooling in the inner regions and of decreasing outer entropy production as the accretion peters out. We propose these radial and time features constitute a cluster Grand Design that we use here to derive a number of predictions. For HE clusters we predict sustained outer temperature profiles. For LEs we expect the outer entropy ramp to bend over; hence the temperature declines before steepening at low z; this feature goes together with an increasing turbulent support, a condition that can be directly probed with the Sunyaev–Zel'dovich effect. We finally discuss the looming out of two intermediate subsets: a wiggled HE at low z that features central temperature profiles retaining imprints of entropy discharged by active galactic nuclei or deep mergers and high-z LEs where the cosmogony/cosmology had little time to enforce a sharp outer entropy bending.

Key words: galaxies: clusters: general – galaxies: clusters: individual (A399, A1656, A2218, A2256) – methods: analytical – X-rays: galaxies: clusters

Online-only material: color figures

1. INTRODUCTION

Rich galaxy clusters, with their overall masses $M \sim 10^{15}\,M_\odot$ and large virial sizes $R \sim$ Mpc,[5] constitute the most recent cosmic structures with high contrast, but still developing at low redshifts. Their gravitationally dominant dark matter (DM) halos contain an appreciable amount $m \approx 0.16\,M$ of hot, diffuse baryons in the form of an intracluster plasma (ICP) at virial temperatures $k_B T \sim GMm_p/10\,R \approx$ several keV and with average densities $n \approx 10^{-3}$ cm^{-3}. The ICP conditions can be probed in X-rays through its strong bremsstrahlung emissions of powers $L_X \propto n^2\,T^{1/2}\,R^3 \approx 10^{44}$–$10^{45}$ erg s^{-1}.

Our main focus here will be on the physics of the ICP and specifically on its "entropy"

$$k \equiv k_B T/n^{2/3}, \tag{1}$$

or better adiabat (see Bower 1997), which is simply related to the true specific entropy s by $\Delta s \equiv 3/2\,\ln k$. The quantity k will conveniently constitute our leading state variable, due to its basic properties: it is *eroded* and eventually erased at the cluster center by radiative cooling; it is *produced* at shock fronts driven both by supersonic inflows across the cluster boundary and by central outflows; it is *conserved* and stratified upon adiabatic compression of the outer intergalactic medium (IGM) into the ICP contained by the DM potential well.

Our scope will be to relate the entropy levels in the ICP to the evolution of the containing DM halos. As to the latter, we will refer to the standard scenario including hierarchical formation and secondary infall, updated by state-of-the-art N-body simulations and analytical works (e.g., Zhao et al. 2003; Fakhouri et al. 2010; Wang et al. 2011). This scenario envisages a first stage of fast collapse and major mergers forming the halo bulk from the top of the initial density perturbation; this is followed by a slow development of the outskirts by accretion of diffuse matter and minor clumps from the perturbation wings (details and further references are given in Appendix A.1). The two stages are separated by the redshift $z_t \approx 0.5$–1 when the circular velocity v_R^2 at the virial boundary attains its maximal value; this epoch leaves a clear imprint in the halo "concentration" parameter $c \equiv R/r_{-2}$ (the ratio of the virial radius to the reference radius in the halo bulk where the DM density slope equals -2) that grows after z_t following $c(z) \approx 3.5\,(1+z_t)/(1+z)$.

After z_t the halos attain a quasi-static equilibrium described by the Jeans equation; the explicit solutions ("α-profiles," with $\alpha = 1.27$ in rich clusters) for the density $\rho(r)$ and the gravitational potential $\Phi(r)$ are given by Lapi & Cavaliere (2009a, 2009b) and recalled in Equation (B3). Note that the physical scales including r_{-2} are modulated by c.

[5] We adopt the standard "concordance" cosmology (Komatsu et al. 2011), for which the virial radius reads $R \approx R_{100} \approx 4\,R_{200}/3 \approx 2\,R_{500}$ in terms of the radii encircling an average overdensity that amounts to 100, 200, and 500, respectively, over the background density in the critical universe.

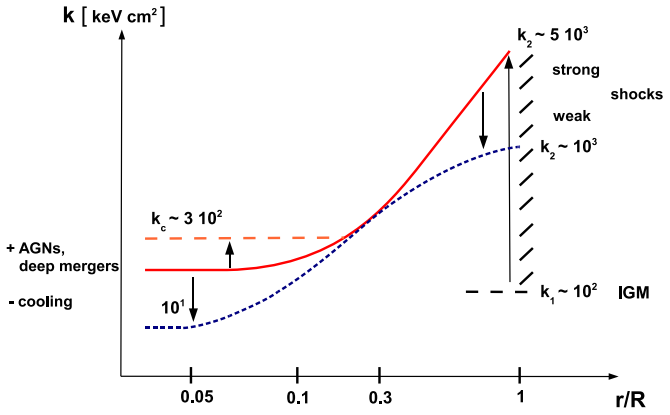

Figure 1. Schematics illustrate our fiducial patterns for the ICP entropy distribution $k(r)$. In the basic pattern (central level plus ramp; red solid line), entropy is raised at the boundary from intergalactic values $k_1 \sim 10^2$ keV cm^2 to high outer levels $k_2 \sim 5 \times 10^3$ keV cm^2 by strong boundary shocks. As the outskirts develop, the shocks weaken and the outer level lowers to $k_2 \lesssim 10^3$ keV cm^2; meanwhile, the central entropy is eroded by radiative cooling down to low levels $k_c \approx 10^1$ keV cm^2 (blue dotted line). On the other hand, blast waves driven by deep mergers may enhance the central levels up to $k_c \sim 3 \times 10^2$ keV cm^2, spread out in the form of an extended floor (orange dashed line).

(A color version of this figure is available in the online journal.)

We will fulfill our purpose with the use of two main tools: basic entropy patterns and the entropy-based equilibrium condition expressed by our Supermodel.

2. ENTROPY PATTERNS

The basic entropy run we expect to apply throughout the ICP can be rendered as a central level k_c connecting to a rising ramp with slope a toward the outer value k_2 in the form (see Tozzi & Norman 2001; Voit 2005)

$$k(r) = k_c + k_2\,(r/R)^a, \tag{2}$$

illustrated in Figure 1 (red solid line). Next we discuss the physical origin of such a minimally structured distribution.

2.1. Central Entropy

In the *central* range $r \lesssim 2 \times 10^2$ kpc, the entropy is initially set at levels $k_c \sim 10^2$ keV cm^2, not much exceeding the levels k_1 prevailing in the IGM (see Ryu et al. 2008; Nicastro et al. 2010). This is because during the initial fast collapse the temperatures in the virialized core are high, at $k_B\,T \approx G\,m_p\,M(<r)/10\,r \sim$ a few keV, but the ICP is dense at $n \sim 10^{-3}$ cm^{-3}, in step with the general overdensities $\delta\rho/\rho \gtrsim 2 \times 10^2$ over the average environment.

Such entropy levels are *eroded* or even erased away following $ds/dt = -s/t_c$, due to the radiative cooling by bremsstrahlung (increasingly dominating over line emission for $k_B T \gtrsim 2$ keV) that makes up the observed X-ray emissions; the associated timescale for a single-phase ICP (see Sarazin 1988) reads $t_c \approx 30\,(k_B T/\mathrm{keV})^{1/2}\,(n/10^{-3}\,\mathrm{cm}^{-3})^{-1}$ Gyr. Thus, cooling may be slow and of little relevance in the low-density outskirts, but is speeded up in the dense central ICP, so that within some 5 Gyr the levels k_c are depressed from $\sim 10^2$ keV cm^2 down to $\sim 10^1$ keV cm^2, at which point cooling becomes so fast as to match the dynamical times $\sim 10^{-1}$ Gyr to the effect of impairing the thermal pressure support; the process is even faster in multiphase ICP with a considerable cold component.

This leads to ICP condensation and to even faster cooling, so starting up an accelerated settling to the cluster center and onto the central galaxies (the classic "cooling catastrophe"), were it not for renewed energy injections (see Binney & Tabor 1995; Cavaliere et al. 2002; Voit & Donahue 2005; Tucker et al. 2007; Hudson et al. 2010). These occur when the accretion reaches down into the galactic nuclei and onto their central supermassive black holes to trigger or rekindle a loop of intermittent starbursts and active galactic nucleus (AGN) activity; in the form of gentle bubbling or moderate outbursts over some 10^{-1} Gyr, this can stabilize the time-integrated k_c at levels of $\sim 10^1$ keV cm^2. Such an enticing scenario is discussed, among others, by Ciotti & Ostriker (2007), McNamara & Nulsen (2007), Conroy & Ostriker (2008), and Churazov (2010). In sum, a cool core constitutes an attractor for the thermal state of the central ICP.

On the other hand, k_c may be *raised* up to levels of several 10^2 keV cm^2 when substantial energy injections ΔE occur into the ICP from violent outbursts of AGNs in central galaxies or even more from deep mergers. These injections drive through the central ICP a blast wave bounded by a leading shock with Mach number gauged by the relation $\mathcal{M}^2 \approx 1 + \Delta E/E$ in terms of the ICP thermal energy $E \approx 2 \times 10^{61}\,(k_B T/\mathrm{keV})^{5/2}$ erg (see Lapi et al. 2005, their Figure 7); a strong shock with $\mathcal{M}^2 \gtrsim 3$ would require injections $\Delta E \gtrsim 2\,E$, i.e., a few tens of keV per particle. This may be the case for deep major mergers, while it is hardly matched by an AGN powered by a supermassive black hole up to $5 \times 10^9\,M_\odot$ with only some 5% of the energy discharged effectively coupled to the ICP (see Lapi et al. 2005).

Blasts that preserve the overall equilibrium may still leave a long-lasting imprint onto the central ICP in the form of an entropy addition spread out to a radius $r_f \approx 10^2$ kpc where the blast has expanded, stalled, and degraded into sound waves. A handy representation (see Fusco-Femiano et al. 2009; see also Appendix B) of the entropy distribution in such conditions is still given by Equation (2) for $r \geqslant r_f$, while a roughly constant level,

$$k(r) = k_c, \tag{3}$$

applies for $r \leqslant r_f$, as illustrated in Figure 1 (orange dashed line). We shall see that conspicuous central wiggles may then appear in the radial temperature profiles if these imprints survive spherical averaging; such features will persist over timescales longer than the blast transit time $\sim$0.3 Gyr if shorter than the cooling time $\sim$5 Gyr.

Stronger if rarer energy injections with $\Delta E \gg E$ can be produced as head-on major mergers following the halo bulk collapse (see McCarthy et al. 2007; Norman 2010) depositing at the center large energies of several tens of keV per particle and entropy levels $\gg 10^2$ keV cm^2; these trigger conditions of severe disequilibrium such as in A754 (see Macario et al. 2011) and A2146 (see Russell et al. 2010), or outright disruption like in MACS J0025.4-1222 (see Bradač et al. 2008) or 1E0657-56 (the "Bullet Cluster," see Clowe et al. 2006).

2.2. Outer Entropy

Supersonic inflows of external IGM drive at the cluster *boundary* $R \sim$ Mpc strong shocks intertwined into a web or layer located at $R_s \approx R$ where accretion feeds on filaments (see Lapi et al. 2005; Voit 2005). These shocks are effective in thermalizing a considerable fraction of the specific energy v_1^2 that the IGM gains as it infalls from the "turnaround" radius $R_{\rm ta}$ to the virial $R \approx R_{\rm ta}/2$ to the effect of providing substantial temperature jumps T_2/T_1 from the IGM values.

These jumps grow with the Mach number squared, $\mathcal{M}^2$, while the density jumps n_2/n_1 saturate to 4 and the post-shock kinetic energy v_2^2/v_1^2 decreases with $\mathcal{M}^{-2}$ in the shock rest frame, cf. Appendix A and Figure 8. As a result, soon after the cluster formation large thermal energies are deposited in the thin ICP at the boundary, with densities still close to the IGM's; there the entropy levels reach up to $k_2 \sim 5 \times 10^3$ keV cm^2.

The bearing of these issues on the ICP physics is focused from the expression derived by Cavaliere et al. (2009) for the value of the entropy slope a_R at the boundary:

$$a_R = 2.5 - 0.5\, b_R. \tag{4}$$

This value (clearly smaller than 2.5) sensitively depends on the ratio $b_R \equiv \mu m_p\, v_R^2/k_B T_2 \gtrsim 1$ of the potential to the ICP thermal energy at $r = R$ (see Lapi et al. 2005). Values $a_R \approx 1.1$ are obtained soon after the bulk collapse, when the inflow is still sustained and strong shocks fully thermalize the infall energy $v_1^2 = 2\,\Delta\Phi$ into three degrees of freedom, and produce post-shock temperatures $k_B T_2 \approx \mu m_p\, v_1^2/3$ (for closer evaluations see Appendices A.3 and A.4). On expressing the potential drop from the turnaround to the shock in the form $\Delta\Phi/v_R^2 \approx 0.57$ (see Cavaliere et al. 2009), the standard values $b_R \approx 3\, v_R^2/2\,\Delta\Phi \approx 2.7$ and $a \approx 1.1$ are obtained (Tozzi & Norman 2001).

Equation (4) is derived as the current boundary value a_R for a, but it clearly also yields the running slope $a(r)$ in the middle range on considering that—in the absence of energy sources—the entropy will be conserved and *stratified* at the values previously produced when the boundary was just at r. In other words, the radial entropy distribution preserves the memory of the past-time development.

As the cluster outskirts grow farther out, the inflows slow down considerably, and do so especially at low z; this straightforwardly occurs when the accretion is drawn from the tapering wings of a DM perturbation over a background lowering under the accelerated cosmic expansion. Thus, the potential drop $\Delta\Phi$ becomes shallower (see Appendix A.1; also Lapi et al. 2010) while the shocks outgrow R to the effect of weakening the shock jumps and lowering T_2 toward the external value T_1. As a result, b_R grows and a decreases toward zero.

A handy representation (see Lapi et al. 2010; see also Appendix B) of the ensuing entropy distribution is still given by Equation (2) inside $r \leqslant r_b$ with $r_b \sim R/3$ (to be discussed in Section 4), while

$$k(r) = k_2\, (r/R)^{a+a'}\, e^{a'\,(R-r)/r_b} \tag{5}$$

applies for $r > r_b$, as illustrated in Figure 1 (blue dotted line). This expression describes a simple linear decline of the slope $a(r)$ with a gradient $a' \equiv (a - a_R)/(R/r_b - 1)$ from the inner value $a \sim 1.1$ to the outer value $a_R < a$.

Such an entropy *bending* takes place on the timescale set by the outskirts development, when the DM halo grows its concentration to values $c \gtrsim 6$ from the initial values $c \approx 3.5$ set soon after the bulk collapse at z_t, e.g., for a cluster collapsed at $z_t \approx 1$ and observed at $z \approx 0.15$ the time elapsed amounts to 6 Gyr.

In sum, the outer ramp flattens and bends over a timescale of several Gyr, while the central level k_c is eroded away by radiative cooling. These two changes are independently driven at far apart locations by quite different processes; what they have in common, though, is their progress in time. So one expectation from our picture is that they should take place *together* as the structures age, a main feature in our cluster classification of Section 5.

3. THE ENTROPY-BASED EQUILIBRIUM

The entropy-based equilibrium of the ICP within the DM gravitational wells is constituted by our Supermodel (see Cavaliere et al. 2009; Fusco-Femiano et al. 2009), with the related straight algebra recapped in Appendix B.

3.1. Thermal Support

There we recall that the linked radial profiles of temperature and density read

$$k_B T(r) = n^{2/3}(r)\, k(r) \propto k^{3/5}(r)\, [1 + 2/5\, b_R\, \mathcal{I}(r)]\,, \tag{6}$$

having used the shorthand $\mathcal{I}(r) \equiv \int_{r/R}^1 dx\, [v_c^2(x)/v_R^2]\, [k(x)/k_2]^{-3/5}/x$ in terms of the circular velocity $v_c^2 \equiv GM/R$ (see also Appendix B, below Equation (B3)). As discussed by Cavaliere et al. (2009), in the outskirts $\mathcal{I}$ is small compared to 1 and the whole factor in square brackets behaves like $(r/R)^{-2\,b_R/5}$; on the other hand, at the center the integral $\mathcal{I} \propto k_c^{-1/4}$ dominates over 1 and scales inversely with the central entropy level k_c.

These temperature and density profiles provide the volume emissivity for bremsstrahlung, proportional to

$$S_X \propto n^2(r)\, T^{1/2}(r) \propto k^{-9/10}(r)\, [1 + 2/5\, b_R\, \mathcal{I}(r)]^{7/2}\,. \tag{7}$$

This constitutes the basis for computing (after spectral-bandpass windowing and projection) the X-ray observables, namely the surface brightness S_X and the emission-weighted temperature; full expressions are given in Appendix B.

We stress that all these profiles for $n(r)$, $T(r)$, and $S_X(r)$ are *linked* together by the underlying entropy distribution. For a relevant example, Equation (6) yields the central scaling laws $T_c \propto k_c^{0.35}$ and $n_c^2\, T_c^{1/2} \propto k_c^{-1.8}$ (see Cavaliere et al. 2009); thus when k_c is *low* the temperature will *dip* and the associated emissivity will *rise* toward the center, features that constitute the signature of the conventional cool-core designation. On the other hand, *high* k_c produce *flat* emissivity profiles together with a wide temperature *plateau*, typical of the conventional non-cool-core designation. Moreover, the central cooling time in single-phase equilibrium may be expressed in terms of the entropy level k_c only to read simply $t_c \approx 0.5\, (k_c/15\,\mathrm{keV\,cm^2})^{1.2}$ Gyr; this implies that high levels of $k_c \approx 150$ keV cm^2 require timescales of order 8 Gyr to be eroded. In the outskirts, instead, the scaling $T(r) \propto r^{7/5\,a_R - 2}$ holds, showing that when $k(r)$ is *bent* down with $a_R \ll 1$, the temperature will fall steeply outward; in simple terms, the profile $T(r) \propto k(r)\, n^{2/3}(r)$ will follow $n^{2/3}(r)$ or steeper when $k(r)$ is nearly constant or even bent down. Meanwhile, the brightness will be flatter at intermediate radii (see Figure 2), and constitutes a simple pointer toward interesting temperature and entropy distributions (see Cavaliere et al. 2011).

An observable independent of X-ray data is provided by the Sunyaev–Zel'dovich (SZ) effect (Sunyaev & Zeldovich 1972); the radial profile of its strength parameter is proportional to the thermal ICP pressure and is written as

$$y(r) \propto n(r)\, T(r) \propto [1 + 2/5\, b_R\, \mathcal{I}(r)]^{5/2}\,. \tag{8}$$

We stress that the Supermodel implies a nearly universal pressure profile (and correspondingly for the SZ effect), since

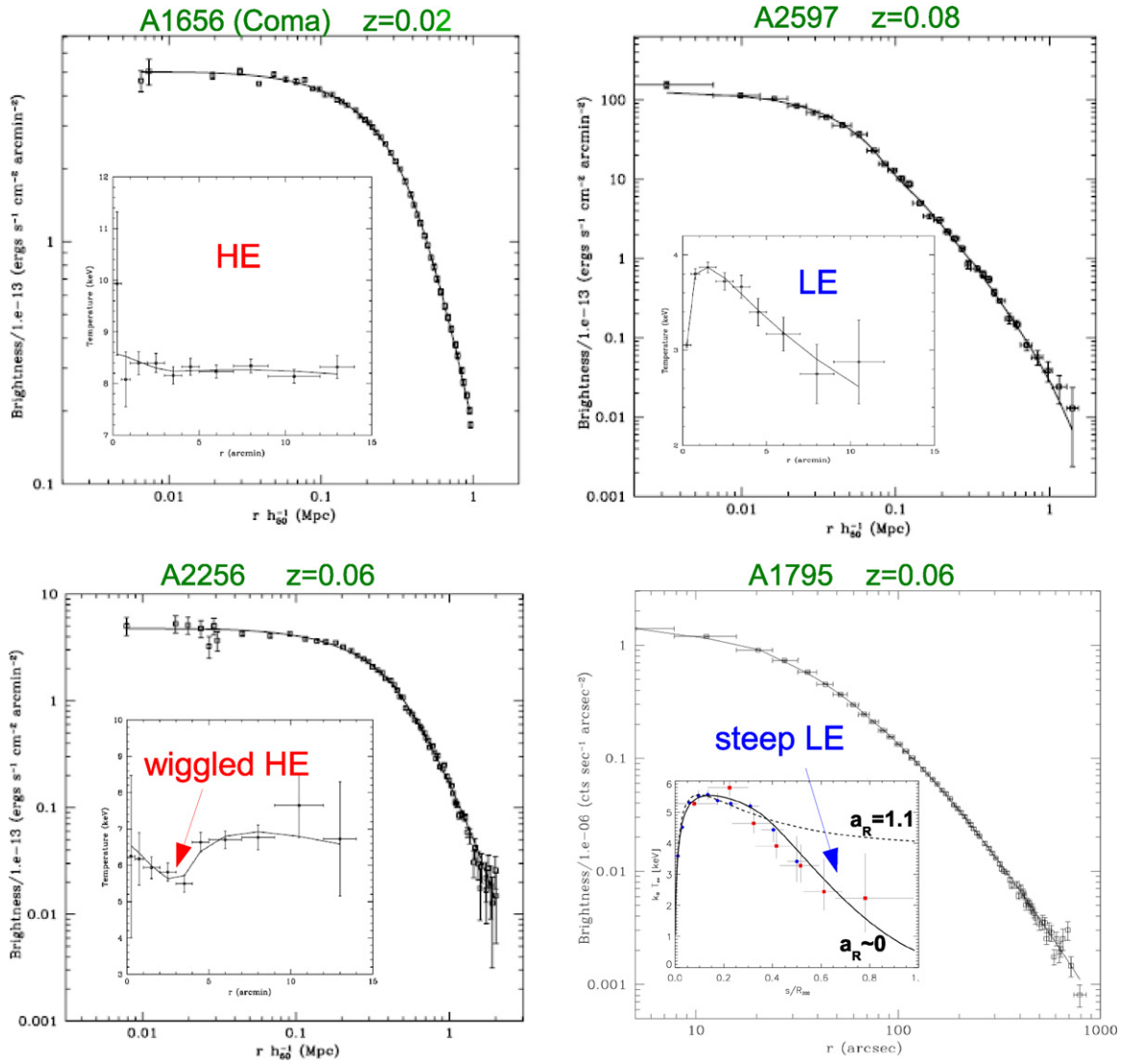

Figure 2. Supermodel fits to the brightness and temperature profiles for the clusters A1656 (top left panel), A2597 (top right), A2256 (bottom left), and A1795 (bottom right). Details are provided in Cavaliere et al. (2009), Fusco-Femiano et al. (2009), and Lapi et al. (2010). In the temperature panel of A1795, the Supermodel fit with a bending entropy profile is reported as a solid line, while the fit with a power-law entropy profile is reported with a dashed line.

(A color version of this figure is available in the online journal.)

the entropy radial dependence is encased into the slowly varying factor $\mathcal{I}(r)$; this is the ultimate origin for the approximate invariance of the pressure profile derived from the X-ray data by Arnaud et al. (2010). Using the inner scaling of n and T with k_c, we find that the scaling $y \propto k_c^{-0.65}$ holds, implying that higher values of y correspond to lower k_c. At the other end, in the outskirts $y \propto r^{2\,a_R-5}$ applies, implying sharper declines in clusters with shallower entropy ramps. Thus, the (projected) SZ effect provides a direct probe of the entropy levels throughout a cluster, and so an independent way for classifying high entropy (HE) and low entropy (LE) types from *Planck* (see Aghanim et al. 2011) and from ground-based instruments.

3.2. Turbulent Support

As argued above, the conditions of LE production are related to mildly supersonic inflows and weak boundary shocks with decreasing Mach number $\mathcal{M}^2 < 3$; we stress that in turn they are conducive to trigger outer subsonic turbulence developing under the drive of relatively more inflow energy $v_2^2/v_1^2 \propto \mathcal{M}^{-2}$ seeping through the weaker shocks (see Cavaliere et al. 2011; also Appendix A.4 for details). The turbulent contribution to equilibrium is conveniently described in terms of the ratio $\delta \equiv p_{\rm nth}/p_{\rm th}$ of the turbulent to thermal pressure. The boundary normalization is consistently set by $\delta_R \propto v_2^2/v_1^2$, while the shape $\delta(r)/\delta_R$ of its inward decline on a scale $\ell \sim 10^2$ kpc is provided by the classic cascade from large "eddies" at the macroscopic coherence length, fragmenting to small eddies where dissipation becomes effective (see Kolmogorov 1941; Monin & Yaglom 1965; see Appendix B.3 for details).

In fact, it turns out that the total pressure $p_{\rm th}+p_{\rm nth} = p_{\rm th}\,(1+\delta)$ can be straightforwardly included in the hydrostatic equilibrium solved by the Supermodel; the result can be described simply in terms of Equation (6), with T and k replaced everywhere (including $\mathcal{I}$) by $\tilde{T} \equiv T\,(1+\delta)$ and by

$$\tilde{k} \equiv k\,(1+\delta). \tag{9}$$

The underlying rationale is that turbulent eddies add to the microscopic thermal degrees of freedom in dispersing and ultimately dissipating the inflow kinetic energy v_2^2 seeped through the shock.

While turbulence is stirred, the thermal pressure required for overall support in the given DM gravitational potential well is decreased. If turbulence were not accounted for, the overall masses estimated from X-rays would tend to be negatively biased compared to the gravitational lensing measurements (Nagai et al. 2007; Lau et al. 2009; Meneghetti et al. 2010; Kawaharada et al. 2010). Meanwhile, the intensity parameter of the volume thermal SZ effect $y(r)$ is lowered relative to the pure thermal equilibrium expression Equation (8) by an explicit factor $1/(1+\delta)$, adding to small corrections to the integrand inside $\mathcal{I}$. Note that such a straightforward lowering is considerably stronger than may result from any reasonable ion–electron disequilibrium at the shock (see the accurate estimates by Wong & Sarazin 2009). Thus, the SZ effect can also provide a *direct* probe of a low thermal pressure, which implies a considerable turbulent component in the cluster outskirts for attaining equilibrium (see Cavaliere et al. 2011). The dearth of outer thermal pressure is indicated by stacked *Wilkinson Microwave Anisotropy Probe* data (see Komatsu et al. 2011); the contribution to such conditions from LEs and HEs will be discussed in a forthcoming paper.

4. TOWARD A CLUSTER LIBRARY

We aim to first construct a library of clusters from extended circularly averaged data; on this basis we aim to introduce a physically meaningful cluster classification scheme and to discuss the connection between the ICP thermal state and the DM halo development. This requires robust fits to the X-ray observables from linked, *consistent* profiles of density and temperature, in order to pinpoint the few independent parameters governing the ICP entropy distribution. Specifically, we adopt the following strategy.

The entropy-based picture of Section 2 (illustrated in Figure 1) suggests the basic entropy distribution of Equation (2), constituting a central level k_c going into a ramp rising with slope $a \approx 1$ toward the outer value k_2. Two relevant and alternative variants may apply: the central floor k_c extends out to a radius r_f and is angled there to the outer ramp, see Equation (3); beyond a radius r_b the ramp bends over to a shallow slope $a_R \ll 1$ joining a low boundary value k_2, see Equation (5). The basic distribution provides a baseline with a minimal number of parameters; the first variant is convenient when central temperatures are high, but wiggles stand out, while the second applies to cases with low central temperature and steep temperature decline into the outer region.

We first insert the basic entropy distribution Equation (2) with free shape parameters k_c and a_R into the Supermodel Equation (6), and derive the radial profiles of density and temperature; the Supermodel algorithm is made available at the URL http://people.sissa.it/~lapi/Supermodel/. We then perform a fit to the projected, emission-weighted temperature data, using a multiparametric χ^2 minimization procedure (e.g., *MPFIT* by Markwardt 2009), and derive the temperature scale T_2 at the boundary (see Equation (B7)). Finally, we fit the surface brightness including the bandpass correction (that requires T_2), and derive the scale n_2 at the boundary (see Equation (B8)). Thus, we obtain also the entropy normalization $k_2 = k_B T_2/n_2^{2/3}$ at the boundary to complete the entropy distribution.

When the χ^2 value of a fit turns out to be large, we proceed to insert in the Supermodel the variant entropy distributions given by either Equation (3) or Equation (5); this adds a further parameter, either r_f (for A644 and A2256) or r_b (for A1795, PKS0745, A2204, A1413). The statistical significance of the added parameter is corroborated by relevant improvements in the reduced χ^2 values (see Table 1). This is further checked with the F-test, which yields a significance level larger than 98% except for A1413 where it is larger than 96%.

Table 1
A Cluster Library

Cluster	Class	k_c (keV cm^2)	r_f/R ($\times 10^{-2}$)	a_R	r_b/R ($\times 10^{-2}$)	c	χ^2
A1795†	LE	15^{+6}_{-6}	...	$-3.43^{+3.36}_{-3.36}$	28^{+2}_{-2}	$8.5^{+1.9}_{-1.9}$	0.3 (2.6)
PKS0745†	LE	15^{+6}_{-6}	...	$-1.78^{+2.68}_{-2.68}$	23^{+3}_{-3}	$7.6^{+1.7}_{-1.7}$	1.4 (4.4)
A2204†	LE	10^{+5}_{-5}	...	$0.16^{+1.41}_{-1.41}$	31^{+7}_{-7}	$5.5^{+1.1}_{-1.1}$	1.1 (2.1)
A1413†	LE	10^{+5}_{-5}	...	$0.36^{+0.31}_{-0.31}$	27^{+7}_{-7}	$8.3^{+1.7}_{-1.7}$	1.2 (1.9)
A2597‡	LE	6^{+18}_{-4}	...	$0.71^{+0.05}_{-0.05}$	...	$7.2^{+5.0}_{-5.2}$	0.3
A2199‡	LE	13^{+6}_{-6}	...	$0.95^{+0.01}_{-0.01}$	...	$6.7^{+1.0}_{-1.0}$	3.1
A1689†‡	LE	105^{+49}_{-49}	...	$0.80^{+0.06}_{-0.06}$	...	$12.4^{+5.3}_{-5.3}$	1.7
A2218⋆	HE	350^{+110}_{-110}	...	$0.8^{+0.1}_{-0.1}$	...	$5.1^{+0.2}_{-0.2}$	0.15
A399⋆	HE	330^{+100}_{-100}	...	$1.0^{+0.1}_{-0.2}$	...	$3.1^{+1.5}_{-1.5}$	1.3
A1656⋆	HE	520^{+160}_{-160}	...	$1.3^{+0.5}_{-0.2}$	...	$3.0^{+0.8}_{-0.8}$	0.7
A644‡	$\widetilde{\text{HE}}$	124^{+120}	$3^{+0.2}_{-0.2}$	$1.1^{+0.1}_{-0.1}$	...	$3.9^{+0.2}_{-0.2}$	0.5 (3.1)
A2256‡⋆	$\widetilde{\text{HE}}$	248^{+224}_{-185}	12^{+4}_{-4}	$1.5^{+0.4}_{-0.3}$	–	$2.7^{+1.7}$	0.9 (2.5)

Notes. Supermodel fits to the X-ray observables performed and/or refined in this work (marked with an ⋆), and in the references Fusco-Femiano et al. (2009; marked with a ‡) and Lapi et al. (2010; marked with a †). The ... in the columns of r_b/R (r_f/R) indicate large (small), irrelevant values. The last column provides the values of the reduced χ^2 for the temperature fits, including r_f or r_b when necessary (in parentheses the values obtained on using the simple power-law entropy run of Equation (2)). Note that for A2218, A399, and A1656 the values $r_f = 12^{+4}_{-4}$, $2^{+0.1}_{-0.1}$, and $4^{+0.2}_{-0.2}$, respectively, come from the centrally flat brightness profile (see discussion by Fusco-Femiano et al. 2009).

We stress that our Supermodel fits are performed over the whole radial range covered by the current X-ray data. In a number of clusters observed by *Suzaku* (e.g., A1795), the X-ray data extend out to approach the virial radius R; in other instances observed by *XMM-Newton* (e.g., A1656), the data are more limited (around R_{500}) and the outer parameters are provided by the Supermodel upon extrapolation, implying larger uncertainties. In the case of PKS0745 the uncertainty is particularly large due to discrepancies between the *XMM-Newton* and *Suzaku* data sets; see the discussion by Eckert et al. (2011).

We note that the shape parameters k_c and a_R may be determined from fitting either the temperature or the brightness profile; the results are consistent within the respective uncertainties, but the value derived from the former is to be preferred whenever extended, high-quality data are available (with the caveats discussed by Eckert et al. (2011) as to anomalous background and by Simionescu et al. (2011) as to effects of possible clumpiness in one sector of the Perseus cluster), since the temperature dominates the brightness in the entropy expression $k \propto T^{7/6} S_X^{-1/3}$ (see Cavaliere et al. 2005).

On the other hand, fits to the X-ray brightness can also provide the DM concentration $c = R/r_{-2}$ that enters the Supermodel formalism through $v_c^2(r)$, while the outer scale R is provided by independent observations such as the red-sequence termination or gravitational lensing. We note that the determination of c is mainly based on the outer brightness data, so is closely independent of the inner entropy distribution. We stress that the Supermodel leads to a fast yet robust evaluation of c from

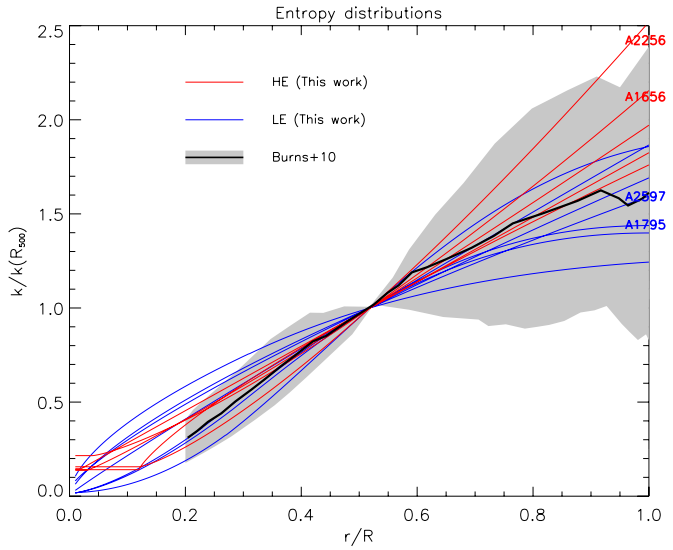

Figure 3. Entropy profiles normalized at R_{500} as determined with the Supermodel for the 12 clusters listed in Table 1; red lines refer to HE and blue lines to LE clusters. In the radial range $r \gtrsim 0.2\,R$ where cooling is negligible, these are overplotted with the outcomes of the nonradiative hydro-simulations by Burns et al. (2010); the black solid line represents the average over their sample of 24 relaxed clusters, with related variance illustrated by the shaded area. The four clusters presented in Figure 2 are labeled.

(A color version of this figure is available in the online journal.)

X-rays only, with results less biased than gravitational lensing by prolateness effects (discussed, e.g., by Corless et al. 2009).

We also note that the few parameters entering the entropy distribution are calibrated from fitting with the Supermodel the observables directly expressed in terms of the radial profiles of $n(r)$ and $T(r)$, with no need for delicate data deprojections (discussed by Yoshikawa & Suto 1999; Cavaliere et al. 2005; Croston et al. 2006; Urban et al. 2011).

The ICP parameters so derived are used here to build up the library of 12 clusters presented in Table 1. Ten of these have been analyzed by us in previous works (Cavaliere et al. 2009; Fusco-Femiano et al. 2009; Lapi et al. 2010), while here we add A399 and refine the analysis of A2218. Examples of Supermodel fits are illustrated in Figure 2.

One may ask to what extent the entropy distributions derived from the Supermodel might depend on the underlying assumptions. These concerns are swept away by Figure 3, where we compare, in the radial range $r \gtrsim 0.2\,R$ where cooling is negligible, the entropy distributions derived from our Supermodel analysis of the 12 clusters listed in Table 1, with the outcomes of the nonradiative hydro-simulations by Burns et al. (2010) for a sample of 24 relaxed massive clusters. Our results are seen to be consistent with the simulation outcomes and their variance, which grows wider into the outskirts.

Moreover, such comparison implies that throughout most of the cluster volume the Supermodel results are robust against the assumptions of spherical symmetry, hydrostatic equilibrium, and purely smooth accretion. In fact, in the inner regions merger-related geometrical asymmetries are smoothed out on a crossing timescale, shorter than the time required by cooling to erase entropy excesses of $\sim 10^2$ keV cm^2. In the middle regions, approximately spherical symmetry of the ICP is indicated by various simulations (e.g., Lau et al. 2011). In the outer regions, the accretion is dominated by minor mergers or truly diffuse matter, as shown in detail by the simulations of Wang et al.

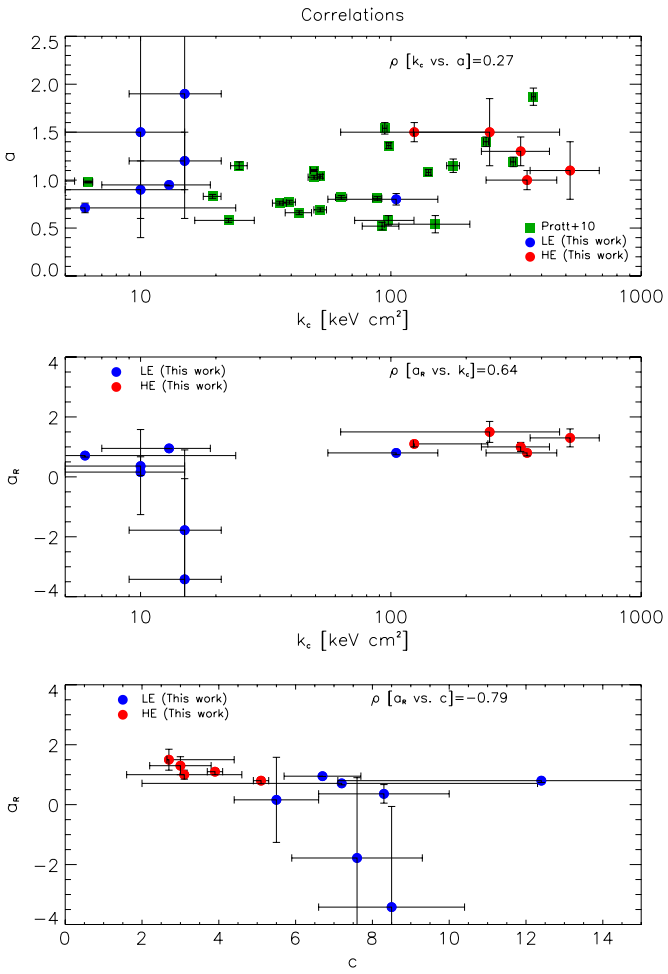

Figure 4. Top panel: central entropy level k_c vs. entropy slope a in the cluster bulk. Dots illustrate our results from the Supermodel analysis of the 12 clusters listed in Table 1 (red dots refer to HEs and blue dots to LEs); squares are from the sample of 29 relaxed clusters by Pratt et al. (2010). Middle panel: central entropy level k_c vs. outer entropy slope a_R; symbols are as above. Bottom panel: the DM concentration c vs. the outer ICP entropy slope a_R; symbols are as above. In all panels the Spearman's rank correlation coefficients ρ for the average data values are reported.

(A color version of this figure is available in the online journal.)

(2011, see their Figure 7). All of this explains why the snapshots provided by our Supermodel fits to the X-ray data are so robust.

5. A CLUSTER GRAND DESIGN

We have divided the 12 clusters listed in Table 1 into two main blocks on the basis of their k_c values being of the order of a few 10^1 or a few 10^2 keV cm^2; within each block, we have ordered the clusters on the basis of their a_R values. It is easily seen that the two main blocks are also divided as to the values of their DM concentration c. The ordering indicates *correlations* between these basic physical parameters quantified in Section 5.1, and suggests an evolutionary *trend* linking the ICP thermal state with the DM development to be discussed in Section 5.2.

5.1. Correlations

In the top panel of Figure 4, we illustrate the central entropy level k_c versus the entropy slope a in the cluster bulk at $R_{500} \approx 0.5\,R$. For cool-core clusters our results (blue dots) from the Supermodel analysis compare well in terms of central

values and their uncertainties with the sample of relaxed, mostly cool-core clusters by Pratt et al. (2010; green squares). It is seen that in terms of the average data values, k_c correlates poorly with a at R_{500}, as quantified by the low value of the Spearman's rank correlation coefficient $\rho \approx 0.27$ (cf. Lupton 1993) both for our and the above authors' samples.

In the middle panel of Figure 4, we illustrate the central levels k_c versus the outer slopes a_R. For a_R we find values close to a for non-cool-core clusters (red dots), but appreciably lower values for cool-core clusters (blue dots). It is seen that a_R correlates well with k_c in terms of the average values; this is quantified by the value of the Spearman's rank correlation coefficient $\rho \approx 0.64$. On the other hand, the often large uncertainties in a_R (related to true uncertainties in the outer X-ray data) and especially in k_c (related also to inner physical complexities) will blur the correlation.

We test to what degree this occurs by running 10^5 Monte Carlo simulations, randomly sampling values of k_c and a_R from Gaussian distributions around their averages, with widths given by their formal $1-\sigma$ uncertainties in both variables; with this conservative treatment the average Spearman's coefficient is lowered to $\rho \approx 0.44$, corresponding to a 9% probability for chance occurrence of the correlation. In addition, we compute that on statistical grounds the probability of "outliers" (objects with $k_c \geqslant 30$ keV cm^2 and $a_R \leqslant 0.6$) is 5% on average, with a formal standard deviation of 22%; this implies that on doubling the size of present sample to 24 objects, one should expect from 1 to 7 outliers. The above outcomes motivate us to investigate in Section 5.2 whether a physical basis underlies the apparent dearth of clusters with high central entropy levels $k_c > 10^2$ keV cm^2 and low outer entropy production $a_R < 1$.

In the bottom panel of Figure 4, we illustrate the outer slopes a_R versus the concentration parameter c, derived with the Supermodel. We find that low values of a_R correspond to high values of c, which mark a long lifetime from the formation z_t to the observation redshift $z \approx 0$ following $c \approx 3.5\,(1+z_t)/(1+z)$. Such an anti-correlation between a_R and c is highly significant for the average data values, with a Spearman's coefficient $\rho \approx -0.79$; on the other hand, the additional uncertainties that also affect c lower it to the conservative value $\rho \approx -0.46$. Again, this outcome stimulates us to investigate any physical dearth of clusters with high concentration $c > 6$ and steep outer slopes $a_R > 1$, and offers a pattern to be confronted with future real and/or virtual data sets.

5.2. Classes

Guided by the above discussion, we submit that all our clusters may be divided into two main classes, defined on the basis of low or high entropy prevailing not only in the inner region but also *throughout* the ICP.

1. HE clusters, featuring high entropy *throughout* the ICP; that is, featuring not only a central level $k_c \approx 3 \times 10^2$ keV cm^2, but also a very high boundary level $k_2 \approx (3\text{–}5) \times 10^3$ keV cm^2 corresponding to a steep entropy ramp with $a \gtrsim 1$ throughout the outskirts. The high values of k_c yield a monotonic temperature profile $T(r)$ throughout, slowly declining from the central plateau into the outskirts. We stress that our class definition includes not only a central non-cool-core state as in the designation introduced by Molendi & Pizzolato (2001) and pursued by Leccardi et al. (2010), but also an associated high level of outer entropy production. We propose that the association arises due to the *young* age of the containing DM halos, marked by low values of the concentrations $c \approx 4$, with a lifetime too short for central entropy to be erased away and any entropy bending to be effective in the outskirts.
2. LE clusters, featuring low entropy *throughout* the ICP; this includes both a *low* central baseline $k_c < 30$ keV cm^2 and a moderate outer level $k_2 \lesssim 10^3$ keV cm^2, so as to imply a ramp bending outward of $r_b/R \gtrsim 0.3$ toward $a(r) < 1$ (see also Hoshino et al. 2010); the outcome is a low central value of T and a *peak* of $T(r)$ at $r/R \lesssim 0.2$ followed by a steep decline outward, particularly effective at low z (e.g., A1795). Our class definition includes not only a central cool-core state as in the standard designation, but also an associated low level of outer entropy production. We propose that the association low k_c–shallow a_R can be traced back to the long lifetime of the containing DM halos, marked by *high* values of the concentrations $c \gtrsim 6$. We relate such a late stage in the outskirts development to dwindling inflows that cause weaker boundary shocks with $\mathcal{M}^2 \lesssim 3$, low entropy production, and a substantial fraction of kinetic energy left over to drive outer turbulent eddies.

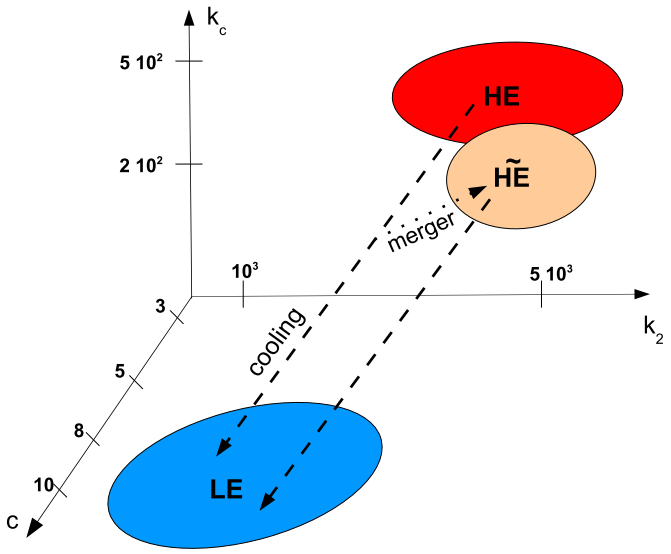

Figure 5. Schematics illustrate the relationships among the cluster classes from the Grand Design.

(A color version of this figure is available in the online journal.)

The low k_c levels of LEs are driven by cooling timescales t_c shorter than the halo dynamical age marked by c. In fact, the divide between LEs and HEs is around $k_c \approx 150$ keV cm^2 corresponding to a cooling time $t_c \approx 8$ Gyr (e.g., the lapse between $z \approx 1$ and $z \approx 0.1$); after this, fast cooling leads to an accelerated progress toward k_c levels that are lower still. Eventually, however, the levels of k_c are likely to be stabilized by two additional physical processes, i.e., intermittent AGN activity and impacts of deep major mergers; two modes are suggested by the broad, possibly double-peaked distribution for the number of clusters with given k_c, as observed by Cavagnolo et al. (2009) and Pratt et al. (2010), and discussed by Cavaliere et al. (2009).

The relationship between the classes is illustrated in the *evolutionary* chart of Figure 5 that represents our cluster Grand Design. This envisages clusters mainly born in an HE state of high entropy, dominated by the fast violent collapse of the halo

bulk and related strong shocks in the infalling gas. Subsequently, on a timescale of several Gyr they progress toward an LE state since both the central entropy is lowered by radiative cooling and the outer entropy bends over because of the weakened shocks and tapering entropy production. The Grand Design envisages that in a number of cases such a sequence may be halted within a few Gyr and *reversed* by late, trailing deep mergers which remold any nascent cool core and *rejuvenate* the central ICP into a higher entropy state.

In fact, these clusters with ICP lingering in such an intermediate state may be conveniently ranked in a subclass labeled $\widetilde{\rm HE}$, distinguished from basic HE by a wiggled central temperature profile. We have shown (see discussion by Fusco-Femiano et al. 2009) that such profiles obtain whenever the central entropy features a floor k_c extended out to a radius $r_f \sim 10^2$ kpc; correspondingly, the central brightness features a particularly flat profile. We recall from Section 2 that such entropy additions are likely imprinted by a blast wave with Mach numbers $\mathcal{M}^2 \gtrsim 3$ launched outward by a head-on impact of a deep merger. When the blast has stalled around r_f and the overall equilibrium in the ICP is recovered, the central entropy is still enhanced to levels up to $k_c \sim 10^2$ keV cm^2, and so is immune to subsequent, weaker AGN-driven blasts. Such an $\widetilde{\rm HE}$ morphology turns out to occur not only in the two cases listed in our Table 1, but also in several more instances of the kind illustrated by Rossetti & Molendi (2010), close to 50% of their non-cool-core clusters; thus we propose that the $\widetilde{\rm HE}$s deserve a subclass status.

Our interpretation of the $\widetilde{\rm HE}$ morphology relates the size r_f to the epoch of the merger responsible for the entropy input; such an epoch is expected to be in between the blast transit time $r_f/\mathcal{M}\,c_s \sim$ some 10^{-1} Gyr and the several Gyr taken by radiation to erode the floor or by central turbulence to blur it. Such a timing ensures an accurate description of the ICP thermodynamics by the Supermodel based on hydrostatic equilibrium. Note also that the ICP attains its equilibrium somewhat faster than the DM does (see Ricker & Sarazin 2001; Lapi et al. 2005), while the circularized data (see Snowden et al. 2008) tend to smooth out limited deviations from spherical hydrostatics (for a detailed discussion see Fusco-Femiano et al. 2009).

6. PREDICTIONS FROM THE GRAND DESIGN

Here, we present other, specific predictions derived from our cluster Grand Design.

1. We expect the HE clusters to feature outer profiles, $T(r)$, declining mildly to a boundary value T_2 still *sustained*. We illustrate in Figure 6 our prediction for such a mild decline in the two HE clusters A1656 and A2256, compared with the currently limited data. Note that for A1656 our Supermodel fit has used only the data of Snowden et al. (2008) out to $r \approx R/3$; our outer prediction agrees with the recent data of Wik et al. (2009) extending out to $R/2$.
2. We expect LE clusters at *low* z to feature particularly *small* values of k_c and *sharply* bent outer entropy profiles. The latter yield *steeply* declining $T(r)$ profiles, as supported by the *Suzaku* observations of a few clusters like A1795; a similar recent case may be constituted by A2142 (see Akamatsu et al. 2011). Low SZ signals and an increasing contribution of outer turbulent support are also expected; relatedly, in these clusters the mass reconstructed from X-ray observations will show systematic *deficits* relative to the gravitational lensing result (see Cavaliere et al. 2011).
3. We expect a *lower* fraction of LEs at *higher* z, reflecting the main evolutionary trend from HEs to LEs envisaged by our Grand Design; this is consistent with the evidence of Santos et al. (2010) based on observing the average surface brightness up to redshift $z \approx 1.3$. When observations of very low surface brightness become feasible, we expect steeper brightness profiles and a milder temperature decline in the outskirts to loom out (see Section 3.1), because for such high-z LEs the cosmology/cosmogony has not had enough time to sharpen the outer entropy bending.

Our picture envisaging LE or HE levels to hold throughout the ICP is consistent with the present dearth of the following pairings: nearby clusters with low k_c levels and high a_R values (that would be located in the upper left strip of the k_c–a_R plane in Figure 4); clusters with high $k_c > 10^2$ keV cm^2 and low $a_R < 1$ (that would be located in the lower right corner of the k_c–a_R plane in Figure 4); inner temperature wiggles in highly concentrated clusters with $c \gtrsim 6$. Wider libraries based on extended, high-quality temperature data will allow the above predictions to be tested. We add that the Supermodel predicts that the projected SZ effects (otherwise closely universal, Section 3.1) to differ between the HE and LE cluster populations, with the latter featuring steeper profiles in the outskirts; in fact, as stated in Section 3.2, in LEs outer turbulence is expected to contribute substantially to the equilibrium, lowering the thermal SZ effect by $1 + \delta$.

7. DISCUSSION AND CONCLUSIONS

We have seen how the cluster thermodynamical state of nearly relaxed clusters can be probed by means of *linked*, robust profiles of density and temperature in the ICP derived from extended X-ray data. We have carried out such a task using the Supermodel formalism with its few, *intrinsic* parameters that modulate the underlying distribution of the specific entropy. On this basis, we have grouped the rich clusters analyzed here into two main classes, LE and HE, depending on the low or high entropy prevailing *throughout* the ICP.

Such classes constitute thermal conditions with long persistence. In fact, HEs with their hot atmospheres are stabilized by long cooling times and stubborn resistance to supersonic flows; LEs are likely stabilized by inner AGN energy injections, while their outskirts evolve slowly as the inflows across the boundary decrease toward low z. The main overall evolutionary course proceeds from HEs to LEs due to erosion of central entropy by cooling, and to reduced production of outer entropy by weakened accretion shocks.

However, such a course may be interrupted or even reversed by large entropy injections from major mergers, particularly frequent at high z; thus, an $\widetilde{\rm HE}$ thermal state sets in, distinguished by wiggles in the central radial temperature distribution. These are interpreted in the Supermodel framework in terms of a sharp entropy floor extending out to $r_f \gtrsim 50$ kpc and with levels k_c around 200 keV cm^2. We consider these as intermediate objects, constituting a subclass contiguous to and blending into the HE main class.

Our overall picture derived from the snapshots condensed in Table 1 *relates* the ICP thermal state to the DM halo development stage, in the form of an inverse correlation between the outer entropy slopes a_R and the halo concentrations c. While the outer ICP thermodynamical age is signaled by the former, the DM dynamical age is marked by the latter, specifically in terms of

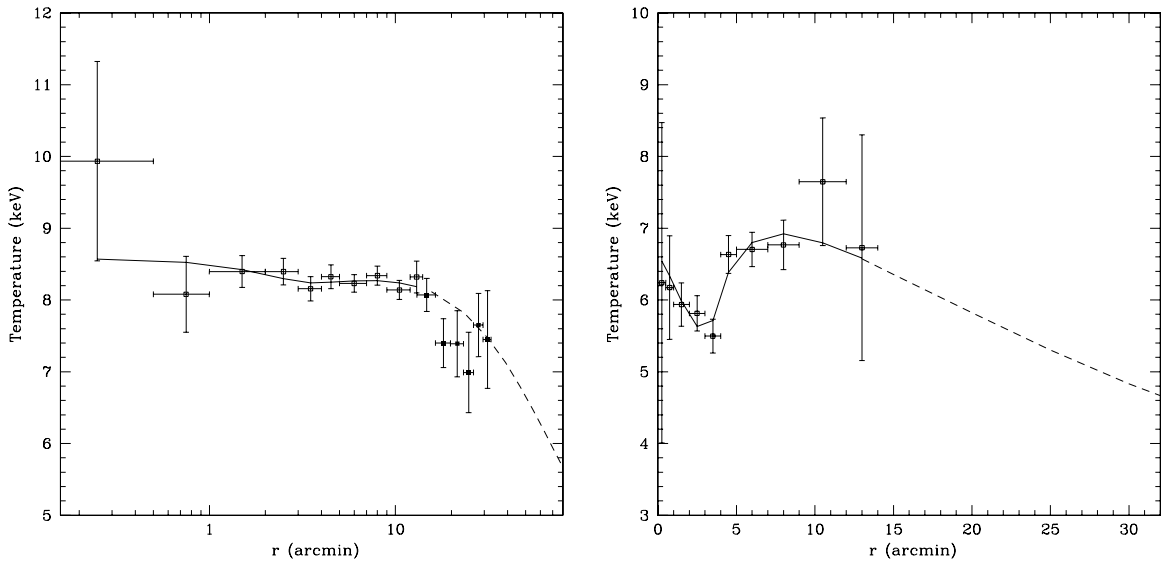

Figure 6. Outer temperature profiles $T(r)$ we predict with the Supermodel from the existing inner/middle data concerning the clusters A1656 (left panel) and A2256 (right panel); data for the former are from Snowden et al. (2008) and Wik et al. (2009), and for the latter from Snowden et al. (2008). The solid line represents our Supermodel fit in the region covered by the data, while the dashed line illustrates our prediction in the outskirts (for A1656 the fit has been performed basing solely on the inner data of Snowden et al. 2008).

$c(z) \approx 3.5\,(1+z_t)/(1+z)$ increasing from the formation z_t to the observation redshift z.

We interpret such a correlation as follows. The LEs are associated with high-c halos, *old* enough to allow the ICP to be affected by deep radiative erosion of their central entropy (producing low k_c values) and by reduced entropy production in the outskirts (shallow a_R or low k_2); the latter effect inescapably depends on large-scale cosmogonical/cosmological evolution, and at given c is more pronounced at low z when reduced accretion is most effective. Conversely, the HEs (and $\widetilde{\text{HE}}$s) are associated with *young* halos of low $c \lesssim 4$. We stress that such central and outer ICP thermal evolutions are independently driven at far apart locations by different processes; what they have in common, though, is their largely parallel progress over comparable timescales of several Gyr.

On the other hand, a reasonable amount of variance in central entropy and in outer bending may produce some intermediate instances; one such case is constituted by A1689 at $z \approx 0.18$, with its still rather high k_c level and intermediate values of its outer entropy slope. As a matter of fact, considerable variance around the average picture will be caused by the well-known scatter in the birth and development of cosmic structures; this affects both the halo collapse redshifts z_t (e.g., Bullock et al. 2001; Wechsler et al. 2006; Klypin et al. 2010) and the subsequent merging histories (e.g., McCarthy et al. 2007; Fakhouri et al. 2010). In particular, A1689 with its mass $M \approx 1.3 \times 10^{15}\,M_\odot$ constitutes a well-studied case of high $z_t \approx 2.5$ as inferred from its high concentration $c \gtrsim 10$ (see Appendix A; also Broadhurst et al. 2008; Lapi & Cavaliere 2009b).

Another source of variance results from the cluster environment; in particular, adjoining filaments with contrasts $\delta\rho/\rho \sim 5$ will enhance diffuse accretion in a rich ambient like a supercluster, so as to delay weakening of shocks and onset of turbulence. This may be the case with one sector out of four in A1689 (see Kawaharada et al. 2010; Molnar et al. 2010) and with A2199 (see Rines et al. 2002), implying the spherically averaged values of a to be higher than in standard LE clusters; the opposite holds true for cluster sectors facing voids.

Additional variance might arise from cold subclumps in sectors of the nearby Virgo and Perseus clusters; this would bias the high surface brightness and the apparent baryonic fraction (see Ettori et al. 1998 versus Simionescu et al. 2011; Urban et al. 2011). On the other hand, such features do not appear to affect most of the clusters collected in Table 1, including instances with steep temperature decline and flat entropy distributions like A1795; for the latter, our Supermodel yields an outer baryonic fraction bounded by 0.14. Similar values have been recently inferred from aimed *Suzaku* observations of A2142 (see Akamatsu et al. 2011).

In LE clusters, we expect *outer* turbulence related to compressive modes to develop under the drive of kinetic energy increasingly seeped through weakening shocks (Cavaliere et al. 2011). *Inner* turbulence, on the other hand, is likely stirred in HE clusters by shear motions associated with the mergers' wakes (e.g., Iapichino et al. 2011). These motions are widely held to accelerate electrons in situ up to Lorentz factors $\gamma \sim 10^4$; the electrons energize strong radiohalos by their synchrotron radiation in cluster-wide magnetic fields of a few μG, with electron lifetimes under 1 Gyr (see Ferrari et al. 2008; Feretti et al. 2011; Brunetti 2011), shorter than the thermal cooling times around 5 Gyr for the center of an HE cluster. On the other hand, in the process of cooling toward an LE state with levels $k_c \lesssim 50$ keV cm^2 the core becomes sufficiently cold as to be sensitive even to lesser mergers. Then temperature wiggles and radiohalos may form together, but the latter will fade much sooner than the former can be eroded away (see Buote 2002; Brunetti et al. 2009; also Rossetti et al. 2011); as a result, we expect more $\widetilde{\text{HE}}$ clusters than radiohalos.

In this paper, we have shown how entropy offers a key to detailed ICP profiles, and a handle to physically relate the ICP state to the DM's (see Section 5.1). In the cases we have analyzed to now, we have identified two main cluster populations, HE and LE (see Section 5.2). We have found the former to feature concentrations $c \approx$ 3–5 associated with a slow outer decline of $T(r)$ from a central plateau, a flat central, and a steep outer brightness; one variant of this pattern is due to the ICP being rejuvenated by mergers, leading to the $\widetilde{\text{HE}}$ subclass. The other

main population is constituted by the LE clusters. We have found these to feature higher concentrations $c \gtrsim 6$, associated with a central brightness spike and low but not vanishing central temperature, and a steep outer decline of $T(r)$ from the inner peak, with a considerable contribution of turbulent support to equilibrium. Such a pattern is generally sharpened toward low z (see Section 6), and implies low outer SZ signals. Finally, our picture leads us to expect a main evolutionary sequence proceeding from HE to LE clusters. The above classification and time developments combine into our cluster Grand Design.

In summary, in the articulated ensemble of galaxy clusters, the entropy-based framework provided by our Grand Design offers a thread toward understanding their basic astrophysics. Specifically, from the X-ray vantage point we interpret the correlations between ICP and DM parameters in terms of synchronization of the central and outer entropy demises, over timescales of several Gyr. Within such a context, variance may be introduced by diverse large-scale environments adjacent to the outskirts, and possibly by multi-phase conditions at the center. Such a variance may blur the synchronized developments, and originate instances *intermediate* between our two main classes. We have identified one such ensemble, the $\widetilde{\rm HE}$ clusters observed at relatively low z. At the other end, $z > 0.5$, our Grand Design raises a specific issue concerning any clusters where central cooling is already advanced (possibly requiring a multi-phase ICP), while entropy production is still high in briskly developing outskirts (see also Section 6). Observations of such objects at the current frontier of cluster astrophysics will constitute a challenging but rewarding aim.

This work has been supported in part by ASI/INAF agreement no. ASI-INAF 1/016/07/0. We thank our referee for stimulating us to include quantitative correlations, and to substantially improve our presentation. We also acknowledge useful discussions with A. Balbi, and with S. Ettori, P. Mazzotta, S. Molendi, and P. Rosati in the context of the meeting "A New Generation of Galaxy Clusters Surveys," 2011 July at the Sexten Center for Astrophysics. A.L. thanks SISSA for warm hospitality.

APPENDIX A

CLUSTER BUILDUP

In this appendix, we collect for the reader's convenience some *basics* of cluster formation, that are used throughout the main text to understand the entropy distribution in the ICP in connection with the halo development stages. Here, our thrust will be to relate these stages to the shape of the initial density perturbation; on basic grounds, such timescales as $t_{\rm coll} \propto (G\,\rho)^{-1/2}$.

In detail, the perturbation shape is conveniently parameterized as $\delta M/M \propto M^{-\epsilon}$, which may be considered a piecewise approximation to a realistically bell-shaped cold DM perturbation. Here, δM represents the mass excess within a shell at the initial comoving radius $r_i \propto M^{1/3}$ enclosing a mass M at background density. Such a shell will progressively detach from the Hubble flow, reach a maximum "turnaround" radius $R_{\rm ta} \propto r_i/(\delta M/M) \propto M^{\epsilon+1/3}$, and collapse back under local gravity to a virialization radius $R \approx R_{\rm ta}/2$.

The virialization occurs when $\delta M/M$ attains the critical threshold $1.69\,D^{-1}(t)$ in terms of the linear growth factor $D(t)$ which depends on the cosmic time t. So the shape parameter ϵ also governs the mass buildup after $M(t) \propto D^{1/\epsilon}(t) \propto t^{d/\epsilon}$, where in the standard cosmology $D(t) \propto t^d$ applies with d lowering from 2/3 to 1/2 as z decreases from above 1 to below 0.5. The corresponding collapse time reads $t_{\rm coll} \equiv M/\dot{M} = \epsilon\, t/d$ for the shell surrounding the mass M. Here, ϵ marks the cosmogonic effect of the perturbation tapering shape; on the other hand, d marks the effects of cosmology at large thinning out the background, and delaying collapse when d approaches 1/2. In many relations that follow, what matters for the effective degree of halo development will be the combined index $\epsilon/d = t_{\rm coll}/t$; values $\epsilon/d \lesssim 1$ apply to the fast collapse of the perturbation bulk, while during the slow outskirts development the accretion rate peters out corresponding to values $\epsilon/d \gtrsim 1$. Note that the transition between the two regimes at z_t corresponds to $\epsilon/d = 1$, i.e., to the collapse time matching the Hubble expansion timescale as per definition; of course, this agrees with the transition epoch recognized in state-of-the-art N-body simulations and semianalytic computations (see Zhao et al. 2003; Diemand et al. 2007; Fakhouri et al. 2010; Genel et al. 2010; Wang et al. 2011). At z_t, the halo concentration takes on the value $c \approx 3.5$ (with minor mass dependence, see Prada et al. 2011) and grows afterward as $c(z) \approx 3.5\,(1+z_t)/(1+z)$.

While the halo develops and the concentration increases, the entropy is produced by shocks in the contained ICP both at the center and at the boundary. The driver for the latter shocks is the external gas inflowing under the pull of the outer gravitational potential well; the inflow varies during cluster development to produce the effects discussed below.

A.1. Decreasing Potential Drops

The potential drop from the turnaround $R_{\rm ta}$ to the shock radius R_s reads

$$\Delta\Phi = -\int_{R_{\rm ta}}^{R_s} dr\,\frac{G\,\delta M}{r^2}. \tag{A1}$$

As the integrand behaves like $\delta M/r^2 \propto M^{1-\epsilon}/r^2 \propto r^{1-3\epsilon}$, one finds

$$\Delta\phi = \frac{1-(R_s/R_{\rm ta})^{3\epsilon-2}}{3\epsilon-2}, \tag{A2}$$

where $\Delta\phi \equiv \Delta\Phi/v_R^2$ is for the drop normalized to the circular velocity scale $v_R^2 = GM(<R)/R$, in fact at radius R_s of the boundary shock. The potential drop as a function of ϵ is illustrated in Figure 7.

A.2. Outgrowing Shock Positions

The position R_s of the shock may be determined from the scaling laws

$$v_1^2 \propto \frac{M}{R_s}\,\Delta\phi\,\dot{M} \propto \rho\, v_1\, R_s^2; \tag{A3}$$

here $M \propto \rho\, R_s^3$ is the overall mass within R_s, v_1 is the infall velocity in the cluster frame, ρ is the background density (we have assumed $n_1 \propto \rho$ and $m \propto M$), and $\Delta\phi$ is the adimensional potential drop described above.

Combining the scaling laws yields

$$R_s \propto \frac{M}{\dot{M}^{2/3}}\,(\Delta\phi)^{1/3} \propto \left(\frac{\epsilon}{d}\right)^{2/3}(\Delta\phi)^{1/3}\,t^{(d/\epsilon+2)/3}, \tag{A4}$$

which, when normalized to the turnaround radius $R_{\rm ta} \propto M^{\epsilon+1/3}$, may be written in the form

$$\frac{R_s}{R_{\rm ta}} \propto \left(\frac{\epsilon}{d}\right)^{2/3}(\Delta\phi)^{1/3}\,t^{-d+2/3}; \tag{A5}$$

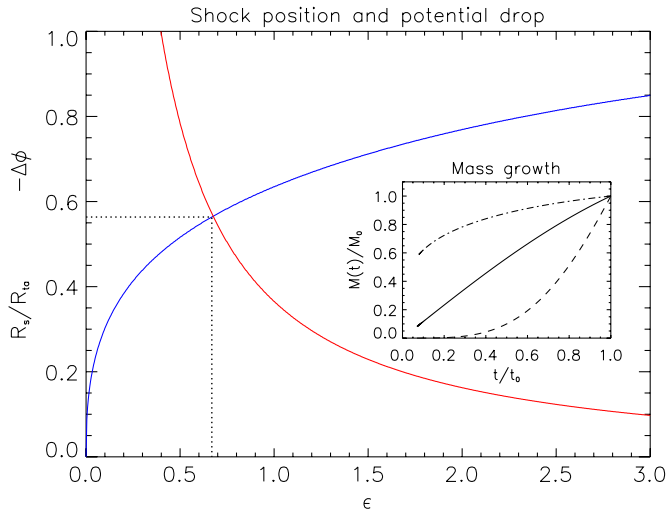

Figure 7. Shock position $R_s/R_{\rm ta}$ relative to the turnaround radius and potential drop $\Delta\phi$ normalized to v_R^2, as a function of the parameter ϵ; the inset illustrates the mass growth $M(t) \propto t^{d/\epsilon}$ for three values of $\epsilon = 1/6$, 2/3, and 3 that span the range $t_{\rm coll}/t = \epsilon/d$ going from 1/4 to 6.

(A color version of this figure is available in the online journal.)

as d takes on values within the narrow range 2/3–1/2, the explicit time dependence is very weak and may be neglected.

Using the expression of $\Delta\phi$ derived in Appendix A.1, the following equation for $x \equiv R_s/R_{\rm ta}$ obtains:

$$\frac{x^3}{1-x^{3\epsilon-2}} = \mathcal{N}\,\frac{(\epsilon/d)^2}{3\epsilon-2}. \tag{A6}$$

The normalization factor $\mathcal{N}$ is set by requiring that at the transition $\epsilon = d$ the potential drop takes on the value $\Delta\phi \approx 0.57$ corresponding to $a \approx 1.1$ after Equation (4) of the main text. This yields a shock radius $R_s \lesssim R \approx R_{\rm ta}/2$ close to the virial boundary during the early stages of cluster buildup that involve high accretion rates, corresponding to $\epsilon \lesssim 1$.

The position of the shock radius and the corresponding values of the potential drop are illustrated in Figure 7. During the early collapse when $\epsilon \ll 1$ applies, we find that the approximations $x \propto \epsilon^{2/5} \to 0$ and $\Delta\phi \propto \epsilon^{-4/5}$ hold. At the other end, during the late outskirts development when $\epsilon \gg 1$ applies, we obtain $x \to 1$ and $\Delta\phi \propto \epsilon^{-2}$; thus the shock positions outgrow the virial boundary to approach the turnaround in the late development stage.

A.3. Decreasing Infall Speeds and Shock Strengths

From the scaling laws Equation (A3) we also derive an expression for the infall velocity (in the cluster frame):

$$v_1 \propto \dot{M}^{1/3}\,(\Delta\phi)^{1/3} \propto \left(\frac{\epsilon}{d}\right)^{-1/3}\,(\Delta\phi)^{1/3}\,t^{(d/\epsilon-1)/3}. \tag{A7}$$

This should be compared with the scaling $c_s \equiv (5\,k_B T_1/3\,\mu m_p)^{1/2} \propto \rho^{1/3}$ of the sound speed in the pre-shock gas; from Equation (A3), we obtain $\rho \propto (\dot{M}/M)^2\,(\Delta\phi)^{-1}$ for the density at the cluster edge to yield

$$c_s \propto \frac{\dot{M}^{2/3}}{M^{2/3}}\,(\Delta\phi)^{-1} \propto \left(\frac{\epsilon}{d}\right)^{-2/3}\,(\Delta\phi)^{-1/3}\,t^{-2/3}. \tag{A8}$$

The ratio of the two quantities reads

$$\frac{v_1}{c_s} \propto \left(\frac{\epsilon}{d}\right)^{1/3}\,(\Delta\phi)^{2/3}\,t^{(d/\epsilon+1)/3}, \tag{A9}$$

and is seen to scale as $\epsilon^{-4/5}\,t^{d/3\epsilon}$ for $\epsilon \ll 1$ and as $\epsilon^{-1}\,t^{1/3}$ for $\epsilon \gg 1$. In other words, strong shocks with $v_1 \gg c_s$ take place during the early collapse of the cluster body, while during the late development of the outskirts the shocks weaken and $v_1 \ll c_s$ applies.

From Equation (A4), we compute the shock speed to be

$$v_s \equiv \dot{R}_s \propto \left(\frac{\epsilon}{d}\right)^{2/3}\,\left(\frac{1}{3}\,\frac{d}{\epsilon}+\frac{2}{3}\right)\,(\Delta\phi)^{1/3}\,t^{(d/\epsilon-1)/3}. \tag{A10}$$

Taking the ratio of the two quantities (Equations (A7) and (A10)) yields the expression

$$\frac{v_s}{v_1} = \frac{1}{3}+\frac{2}{3}\,\frac{\epsilon}{d}. \tag{A11}$$

This takes on values around 1/3 during the early collapse when $\epsilon \ll 1$; it grows during the late outskirts development when $\epsilon \gg 1$, since v_1 vanishes while v_s decreases toward its limiting value given by the sound speed c_s. Note the ubiquitous appearance in the DM dynamics of the key quantity $\Delta\phi$, which will also appear directly in the ICP equilibrium condition.

A.4. Weakening Shocks and Increasing Seepage

In the main text, we discuss how the boundary shocks weaken as the cluster outskirts develops; meanwhile, an increasing fraction of kinetic energy seeps through them. Next we explain why.

The jump conditions for entropy, temperature, and density across a shock front can be written (Landau & Lifshitz 1959) as

$$\frac{k_2}{k_1} = \frac{T_2/T_1}{(n_2/n_1)^{2/3}} \quad \text{with} \tag{A12}$$

$$\frac{T_2}{T_1} = \frac{5}{16}\,\frac{\tilde{v}_1^2}{c_s^2}+\frac{7}{8}-\frac{3}{16}\,\frac{c_s^2}{\tilde{v}_1^2}, \quad \frac{n_2}{n_1} = \frac{\tilde{v}_1}{\tilde{v}_2} = \frac{4}{1+3\,c_s^2/\tilde{v}_1^2}.$$

The suffixes 1 and 2 indicate pre- and post-shock values, while quantities with a tilde refer to the shock rest frame (where the shock velocity $\tilde{v}_s$ is zero by construction); in addition, $\mathcal{M} \equiv \tilde{v}_1/c_s \geqslant 1$ is the Mach number of the accretion shock. The behavior of these quantities as a function of $\mathcal{M}$ is illustrated in Figure 8.

In the cluster frame, the shock velocity v_s differs from zero, and the upstream and downstream bulk velocities are given by $\tilde{v}_{1,2} = v_{1,2} + v_s$. Using Equation (A10), we work out the ratio v_2/v_1 to be

$$\frac{v_2}{v_1} = \frac{1-3\,v_s/v_1}{4}+\frac{3}{4}\,\frac{c_s^2/v_1^2}{1+v_s/v_1}. \tag{A13}$$

The above results are summarized as follows. During the early collapse of the cluster body with $\epsilon \ll 1$, *strong* shocks with $v_1/c_s \gg 1$ and $v_s \simeq v_1/3$ hold; these imply high post-shock temperatures $k_B T_2 \simeq \mu m_p\,v_1^2/3 \propto \epsilon^{-6/5}$ and low bulk post-shock velocities $v_2 \propto \epsilon^{3/5} \simeq 0$. On the other hand, during the late development of the cluster outskirts with $\epsilon \gg 1$, *weak* shocks with $v_1/c_s \ll 1$ and $v_s \simeq c_s$ occur to yield low $T_2 \simeq T_1$ and $v_2 \simeq v_1 \propto \epsilon^{-1}$.

Thus, as the cluster buildup progresses from bulk collapse to outskirts development, at the boundary the thermal post-shock energy $k_B T_2$ monotonically *decreases*, but the bulk energy v_2^2 seeping through the shock to drive turbulence first increases up to a *maximum*; eventually, however, it decreases when the accretion becomes transonic.

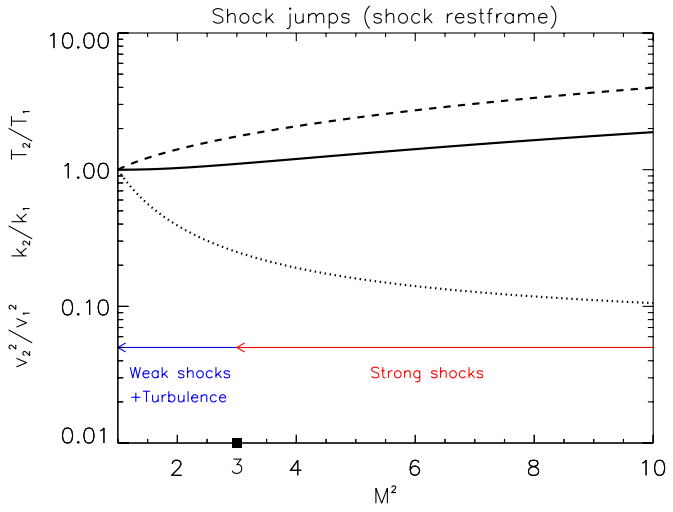

Figure 8. Plot of the shock jumps k_2/k_1, v_2^2/v_1^2, and T_2/T_1 as a function of the squared Mach number $\mathcal{M}^2$ in the shock rest frame; note that the divide between strong and weak shocks (associated with the onset of turbulence) is around $\mathcal{M}^2 = 3$. During a cluster's evolution, the outskirts condition progresses from right to left.

(A color version of this figure is available in the online journal.)

A.5. Specific Clusters

In terms of numerical values, the halo of a typical HE cluster observed at $z \approx 0.1$ collapses at $z_t \approx 0.5$, developing a concentration $c \approx 4$. On the other hand, the halo of a typical LE cluster observed at $z \approx 0.1$ collapses at $z_t \approx 1$; during the evolution ϵ increases from initial values close to 0.3 to values around 0.6 at $z \approx 0.3$, and to 1 on moving to $z \approx 0.1$; meanwhile, its concentration increases from initial values around 3.5 to values around 5 at $z \approx 0.3$, and around 7 at $z \approx 0.1$.

In parallel, for a relaxed, long-lived LE cluster the prevailing Mach numbers decline from $\mathcal{M}^2 \approx 10$ to 3 and then toward 1 at low z, while the ratio v_2^2/v_1^2 increases from 10% to 30% with a correspondingly high outer turbulence level, and then decreases again toward a few percent.

Finally, one borderline instance is provided by the LE cluster A1689 at $z \approx 0.18$; its high concentration $c \approx 10$ implies the collapse redshift $z_t \approx 2.5$, particularly high for its mass $M \approx 1.3 \times 10^{15}\, M_\odot$. The other borderline instance is provided by the HE cluster A2218, again at $z \approx 0.18$; its concentration $c \approx 5$ implies the collapse redshift $z_t \approx 0.7$.

APPENDIX B

THE ICP SUPERMODEL

Here, we recap the basics of our ICP Supermodel introduced in Section 3 (see Cavaliere et al. 2009; Fusco-Femiano et al. 2009; Lapi et al. 2010). The robust snapshots it provides guide our classification of cluster classes, and establish relationships between them to constitute the cluster Grand Design.

In equilibrium conditions, the DM gravitational pull is withstood by the gradient of the thermal ICP pressure p to yield

$$-\frac{GM(<r)}{r^2} = \frac{1}{m_p\, n(r)}\,\frac{dp(r)}{dr} = -\frac{5\,k^{3/5}(r)}{2\,\mu m_p}\,\frac{d}{dr}\left[\frac{k_B T(r)}{k^{3/5}(r)}\right]. \quad \text{(B1)}$$

To begin with, in the second equality we have considered only thermal pressure $p = n\,k_B T/\mu$, expressed in terms of the specific entropy $k \equiv k_B T/n^{2/3}$; in the main text the entropy distribution $k(r)$ is related to definite physical processes: it is conserved by adiabatic compressions, produced at shock fronts, eroded by radiative cooling (nonthermal, turbulent support is dealt with in Appendix B.3).

Equation (B1) shows how, given the potential well, the ICP disposition is set by the entropy distribution $k(r)$. In fact, it constitutes a first-order linear differential equation for $T(r)$, which solves to give the profile

$$\bar{T}(r) = \bar{k}^{3/5}(\bar{r})\left[1 + \frac{2}{5}\,b_R \int_{\bar{r}}^{1} \frac{d\bar{r}'}{\bar{r}'}\,\bar{v}_c^2(\bar{r}')\,\bar{k}^{-3/5}(\bar{r}')\right], \quad \text{(B2)}$$

while the self-consistent density profile follows $\bar{n}(\bar{r}) = [\bar{T}(\bar{r})/\bar{k}(\bar{r})]^{3/2}$. Here, variables with a bar are normalized to their boundary values at $r = R$, while $b_R \equiv \mu m_p\, v_R^2/k_B T_2$ expresses in the solution the boundary condition T_2 provided by the shock jumps.

The squared circular velocity $\bar{v}_c^2(\bar{r}) \equiv \bar{M}(<\bar{r})/\bar{r}$ depends on the DM mass distribution. For the latter, we use our α-profiles derived from the Jeans equation (see Lapi & Cavaliere 2009a, 2009b, 2011); the corresponding density profile reads

$$\bar{\rho}(\bar{r}) = \bar{r}^{-\tau}\left[\frac{1 + w\,c^\eta}{1 + w\,(c\,\bar{r})^\eta}\right]^\xi, \quad \text{(B3)}$$

where $\tau \approx 0.76$, $\eta \approx 0.58$, $\xi \approx 4.56$, and $w = -(2-\tau)/(2-\tau-\eta\xi) \approx 0.88$ are constants with values suitable for rich clusters. Note that the standard Navarro–Frenk–White profile corresponds instead to $\tau = 1$, $\eta = 0$, $\xi = 2$, and $w = 1$. It is seen how the density profile is modulated by c (the standard concentration parameter of the DM halo defined in Section 1 of the main text), and particularly so in the outskirts. *IDL* and *FORTRAN* algorithms to implement the above equations can be found at the URL http://people.sissa.it/~lapi/Supermodel/.

We stress that the standard models for the ICP distribution constitute useful approximations to the Supermodel results (e.g., Cavaliere & Fusco-Femiano 1976; Sarazin 1988); specifically, the isothermal β-model applies in central regions with high central level k_c, while the polytropic model $k(r) \propto n^{\Gamma-5/3}(r)$ with index $\Gamma \approx 1.2$ applies in outer regions where $n(r)$ drops quickly and the temperature $T(r)$ undergoes a mild decline.

In a nutshell, LE levels throughout the clusters allow the ICP thermal velocity dispersion $T(r)$ to passively *mirror* the profile of the DM velocity dispersion $\sigma^2(r)$, sharing its radial run with a middle peak and a decline on both sides (as shown by Cavaliere et al. 2009, and confirmed by Hansen et al. 2010). This is because the DM and the passive ICP (in the absence of entropy additions) settle to a comparable equilibrium within the *common* gravitational potential well. Conversely, HE levels at the center cause the ICP to resist gravitational compressions, and $T(r)$ to maximally *depart* from $\sigma^2(r)$, so as to feature a monotonic increase inward to a central plateau.

B.1. Entropy Distributions Implemented

Here, we describe the radial entropy distributions $k(r)$ implemented in the Supermodel, following the physical motivations given in Section 2 of the main text. As also discussed there, which of the distributions is convenient to try first may be decided a priori from a quick look at the inner temperatures observed in X-rays.

For HE clusters (whose inner temperature profile is flat), we adopt the distribution

$$\bar{k}(\bar{r}) = \bar{k}_c + (1 - \bar{k}_c)\,\bar{r}^a; \quad \text{(B4)}$$

this renders an outward rise with uniform slope a from a central level $\bar{k}_c$ (see Figure 1, red solid line).

For HE clusters (whose inner temperature profile shows sharp wiggles), we adopt the distribution

$$\bar{k}(\bar{r}) = \begin{cases} \bar{k}_c & \text{for } \bar{r} \leqslant \bar{r}_f, \\ \bar{k}_c + (1-\bar{k}_c)\,[(\bar{r}-\bar{r}_f)/(1-\bar{r}_f)]^a & \text{for } \bar{r} > \bar{r}_f. \end{cases} \tag{B5}$$

This represents a floor with level $\bar{k}_c$ extending out to a radius r_f, followed by an outward rise with uniform slope a (see Figure 1, orange dashed line).

For LE clusters (whose inner temperature profiles show an outward rise up to a maximum and then a decline), we implement the distribution

$$\bar{k}(\bar{r}) = \begin{cases} \bar{k}_b\ (\bar{r}/\bar{r}_b)^a & \text{for } \bar{r} \leqslant \bar{r}_b, \\ \bar{r}^{a+a'}\, e^{a'\,(1-\bar{r})/\bar{r}_b} & \text{for } \bar{r} > \bar{r}_b, \end{cases} \tag{B6}$$

where $\bar{k}_b \equiv \bar{r}_b^{a+a'}\, e^{a'\,(1-\bar{r}_b)/\bar{r}_b}$ applies to ensure continuity at $r = r_b$. This renders an outward rise with uniform slope a out to a radius r_b, and then a progressive bending follows with a linear decline of the slope, with the gradient $a' \equiv (a - a_R)\,\bar{r}_b/(-\bar{r}_b+1)$ down to the boundary value a_R (see Figure 1, blue dotted line).

B.2. Observables and Parameter Counting

In connection with Section 4, we detail how from $T(r)$ and $n(r)$ we proceed to compute the profiles of the X-ray and SZ observables. Specifically, the emission-weighted temperature is given by

$$\langle T(\bar{w})\rangle = T_2\,\frac{\int_0^{\bar{r}} d\bar{\ell}\bar{n}^2\,\Lambda[\bar{T}]\,\bar{T}}{\int_0^{\bar{r}} d\bar{\ell}\bar{n}^2\,\Lambda[\bar{T}]}, \tag{B7}$$

where $\bar{r} = \sqrt{1-\bar{w}^2}$ is expressed in terms of the projected radius $\bar{w}$; here $\Lambda[T]$ is the cooling function, with a typical dependence $\Lambda \propto T^{1/2}$ for hot clusters with average $k_B T \gtrsim 2$ keV.

The brightness distribution is given by

$$S(\bar{w}) = n_2^2\, R \int_0^{\bar{r}} d\bar{\ell}\bar{n}^2\,\Lambda[\bar{T}]\,F[E_H, E_L, T], \tag{B8}$$

where the factor $F[E_H, E_L, T] \simeq e^{-E_L/k_B T(r)} - e^{-E_H/k_B T(r)}$ takes into account specific instrumental bands $E_H - E_L$.

Fitting these expressions to the observations enables us to pin down the following parameters and scales. From the profile normalizations we determine the ICP *scales* n_2 and T_2, and the DM scale R (if not independently given by observations of galaxy dynamics, "red-sequence" termination, and gravitational lensing).

From the profile *shapes* one can determine not only the ICP *parameters* describing the entropy run, but also the DM concentration parameter c, when not independently provided by gravitational lensing. For HE clusters two ICP parameters are needed, i.e., the central level k_c and the slope a; for LE clusters three ICP parameters are needed, i.e., the outer value of the slope a_R, the average derivative a' of the slope, and the radius r_b; finally, for the HE clusters three parameters are needed, i.e., the level k_c and the extension r_f of the central floor, and the outer slope a.

A preliminary guideline as to which entropy shape is conveniently tried first is provided by a quick look at the gross temperature run at the center and in the outskirts, as discussed in Section 3. A posteriori, the values of the reduced χ^2 of the fits provide a final check.

An independent observable is provided by the Comptonization parameter that marks the strength of the SZ effect; it can be expressed as

$$y(\bar{w}) = n_2\, T_2\, R \int_0^{\bar{r}} d\bar{\ell}\bar{n}\,\bar{T}. \tag{B9}$$

In the near future interferometric instruments such as ALMA (see http://science.nrao.edu/alma/index.shtml) will provide measurements of comparable sensitivity and resolution to the present X-ray instrumentation on board *XMM-Newton* and *Chandra*.

B.3. Turbulent Support

In connection with Section 3.2, we explain how the Supermodel can be readily extended to cover the ICP equilibrium when nonthermal, turbulent support contributes in addition to thermal pressure (see Cavaliere et al. 2011). The relevant quantity is provided by the ratio $\delta(r) \equiv p_{\rm nth}/p_{\rm th}$ of turbulent to thermal pressure or, equivalently, by the ratio $\delta/(1+\delta)$ of turbulent to total pressure $p_{\rm tot} = p_{\rm th}\,(1+\delta)$.

We expect onset of turbulence in the outskirts of relaxed LE clusters (cf. Equation (A13)), where weakening accretion shocks leave over an appreciable bulk energy to drive turbulent motions with maximal amplitude $\delta_R \approx (v_2/v_1)^2$ up to 30%–40% at the virial radius. In fact, these motions start up with a coherence length $L \sim R/2$ set by the pressure scale height or by shock segmentation enforced by the adjoining filamentary structure, and then fragment into a dispersive cascade over the "inertial range" to sizes ℓ where dissipation begins. In the ICP context the dissipation scale is written as $\ell \sim (c_2/\tilde{v})^{3/4}\,\lambda_{\rm pp}\,(L/\lambda_{\rm pp})^{1/4}$ in terms of the ion collisional mean free path $\lambda_{\rm pp} \approx 50$ kpc and of the ratio $\tilde{v}/c_2$ of the turbulent rms speed to that of sound. For *subsonic* turbulence with $\tilde{v}/c_2 \lesssim 1/3$, the relevant scale ℓ somewhat exceeds $\lambda_{\rm pp} \sim 100$ kpc. This behavior may be rendered in terms of the simple functional shape

$$\delta(r) = \delta_R\, e^{-(R-r)^2/\ell^2}, \tag{B10}$$

which decays on the *scale* ℓ inward of a round plateau, a smoothed out representation of the inertial range. This provides the gradient of the turbulent pressure.

In fact, the equation of hydrostatic equilibrium in the presence of turbulent support will contain the total pressure in the general form $p_{\rm th}(r)\,[1+\delta(r)]$, while the thermal component is still expressed as $p_{\rm th}(r) \propto k(r)\,n^{5/3}(r)$. On noting that $p_{\rm tot} = p_{\rm th}\,(1+\delta) = n\,k_B\tilde{T}/\mu$ with $\tilde{T} \equiv T\,(1+\delta)$, it is convenient to introduce the *extended* entropy

$$\tilde{k} \equiv k\,(1+\delta). \tag{B11}$$

This quantity renders the conversion of kinetic energy into random energy at two levels: the microscopic one given by the standard k and the dispersion into turbulent "eddies" given by $k\delta$. It is easily checked that in these terms the solution has the same form as Equation (B2).

It turns out that the profiles of emission-weighted temperature are little affected by turbulence (see Cavaliere et al. 2011); on the other hand, the thermal SZ effect is lowered to $\tilde{y} \equiv y/(1+\delta)$. Finally, including turbulence in the equation of hydrostatic equilibrium brings the total mass reconstructed from X-rays

into agreement with the findings from simulations and with that measured via gravitational lensing observations (see Nagai et al. 2007; Lau et al. 2009; Meneghetti et al. 2010; Cavaliere et al. 2011).

REFERENCES

Aghanim, N., Arnaud, M., Ashdown, M., et al. 2011, A&A, in press (arXiv:1101.2043)
Akamatsu, H., Hoshino, A., Ishisaki, Y., et al. 2011, PASJ, in press (arXiv:1106.5653)
Arnaud, M., Pratt, G. W., Piffaretti, R., et al. 2010, A&A, 517, 92
Binney, J., & Tabor, G. 1995, MNRAS, 276, 663
Bower, R. G. 1997, MNRAS, 288, 355
Bradač, M., Allen, S. W., Treu, T., et al. 2008, ApJ, 687, 959
Broadhurst, T., Umetsu, K., Medezinski, E., et al. 2008, ApJ, 685, L9
Brunetti, G. 2011, Mem. SAlt, 82, 515
Brunetti, G., Cassano, R., Dolag, K., et al. 2009, A&A, 507, 661
Bullock, J. S., Kolatt, T. S., Sigad, Y., et al. 2001, MNRAS, 321, 559
Buote, D. A. 2002, in Merging Processes in Clusters of Galaxies, ed. L. Feretti, I. M. Gioia, & G. Giovannini (Dordrecht: Kluwer), 79
Burns, J. O., Skillman, S. W., & O'Shea, B. W. 2010, ApJ, 721, 1105
Cavagnolo, K., Donahue, M., Voit, G. M., et al. 2009, ApJS, 182, 12
Cavaliere, A., & Fusco-Femiano, R. 1976, A&A, 49, 137
Cavaliere, A., Lapi, A., & Fusco-Femiano, R. 2011, A&A, 525, 110
Cavaliere, A., Lapi, A., & Fusco-Femiano, R. 2009, ApJ, 698, 580
Cavaliere, A., Lapi, A., & Rephaeli, Y. 2005, ApJ, 634, 784
Cavaliere, A., Lapi, A., & Menci, N. 2002, ApJ, 581, L1
Churazov, E. 2010, in Galaxy Clusters: Observations, Physics and Cosmology, http://www.mpa-garching.mpg.de/∼clust10
Ciotti, L., & Ostriker, J. P. 2007, ApJ, 665, 1038
Clowe, D., Bradač, M., Gonzalez, A. H., et al. 2006, ApJ, 648, L109
Conroy, C., & Ostriker, J. P. 2008, ApJ, 681, 151
Corless, V. L., King, L. J., & Clowe, D. 2009, MNRAS, 393, 1235
Croston, J. H., Arnaud, M., Pointecouteau, E., & Pratt, G. W. 2006, A&A, 459, 1007
Diemand, J., Kuhlen, M., & Madau, P. 2007, ApJ, 667, 859
Eckert, D., Molendi, S., Gastandello, F., & Rossetti, M. 2011, A&A, 529, 133
Ettori, S., Fabian, A. C., & White, D. A. 1998, MNRAS, 300, 837
Fakhouri, O., Ma, C.-P., & Boylan-Kolchin, M. 2010, MNRAS, 406, 2267
Feretti, L., Giovannini, G., Govoni, F., & Murgia, M. 2011, in IAU Symp. 274, Advances in Plasma Astrophysics, ed. A. Bonanno & A. Kosovichev (Cambridge: Cambridge Univ. Press), 340
Ferrari, C., Govoni, F., Schindler, S., Bykov, A. M., & Rephaeli, Y. 2008, Space Sci. Rev., 134, 93
Fusco-Femiano, R., Cavaliere, A., & Lapi, A. 2009, ApJ, 705, 1019
Genel, S., Bouché, N., Naab, T., Sternberg, A., & Genzel, R. 2010, ApJ, 719, 229
Hansen, S. H., Macció, A. V., Romano-Diaz, E., et al. 2010, ApJ, 734, 62
Hoshino, A., Henry, J. P., Sato, K., et al. 2010, PASJ, 62, 371
Hudson, D. S., Mittal, R., Reiprich, T. H., et al. 2010, A&A, 513, 37
Iapichino, L., Schmidt, W., Niemeyer, J. C., & Merklein, J. 2011, MNRAS, 414, 2297
Kawaharada, M., Okabe, N., Umetsu, K., et al. 2010, ApJ, 714, 423
Klypin, A., Trujillo-Gomez, S., & Primack, J. 2010, ApJ, 740, 102
Kolmogorov, A. 1941, Dokl. Akad. Nauk SSSR, 30, 301
Komatsu, E., Smith, K. M., Dunkley, J., et al. 2011, ApJS, 192, 18
Landau, L. D., & Lifshitz, E. M. 1959, Fluid Mechanics (Oxford: Pergamon)
Lapi, A., & Cavaliere, A. 2009a, ApJ, 692, 174
Lapi, A., & Cavaliere, A. 2009b, ApJ, 695, L125
Lapi, A., & Cavaliere, A. 2011, Adv. Astron., 172, 903429
Lapi, A., Cavaliere, A., & Menci, N. 2005, ApJ, 619, 60
Lapi, A., Fusco-Femiano, R., & Cavaliere, A. 2010, A&A, 516, 34
Lau, E. T., Kravtsov, A. V., & Nagai, D. 2009, ApJ, 705, 1129
Lau, E. T., Nagai, D., Kravtsov, A. V., & Zentner, A. R. 2011, ApJ, 734, 93
Leccardi, A., Rossetti, M., & Molendi, S. 2010, A&A, 510, 82
Lupton, R. 1993, Statistics in Theory and Practice (Princeton, NJ: Princeton Univ. Press)
Macario, G., Markevitch, M., Giacintucci, S., et al. 2011, ApJ, 728, 82
Markwardt, C. B. 2009, in ASP Conf. Ser. 411, Astronomical Data Analysis Software and Systems XVIII, ed. D. A. Bohlender, D. Durand, & P. Dowler (San Francisco, CA: ASP), 251
McCarthy, I. G., Bower, R. G., Balogh, M. L., et al. 2007, MNRAS, 376, 497
McNamara, B. R., & Nulsen, P. E. J. 2007, ARA&A, 45, 117
Meneghetti, M., Rasia, E., Merten, J., et al. 2010, A&A, 514, 93
Molendi, S., & Pizzolato, F. 2001, ApJ, 560, 194
Molnar, S. M., Chiu, I.-N., Umetsu, K., et al. 2010, ApJ, 724, L1
Monin, A. S., & Yaglom, A. M. 1965, Statistical Hydromechanics (Moscow: Nauka)
Nagai, D., Kravtsov, A. V., & Vikhlinin, A. 2007, ApJ, 668, 1
Nicastro, F., Krongold, Y., Fields, D., et al. 2010, ApJ, 715, 854
Norman, M. 2010, in Astrophysics of Galaxy Clusters, Int. School of Physics Enrico Fermi, Vol. 172, ed. A. Cavaliere & Y. Rephaeli (Amsterdam: IOS & Bologna: SIF), 51
Prada, F., Klypin, A. A., Cuesta, A. J., et al. 2011, MNRAS, submitted (arXiv:1104.5130)
Pratt, G. W., Arnaud, M., Piffaretti, R., et al. 2010, A&A, 511, 85
Ricker, P. M., & Sarazin, C. L. 2001, ApJ, 561, 621
Rines, K., Geller, M. J., Diaferio, A., et al. 2002, AJ, 124, 1266
Rossetti, M., Eckert, D., Cavalleri, B. M., et al. 2011, A&A, 532, 123
Rossetti, M., & Molendi, S. 2010, A&A, 510, 83
Russell, H. R., Sanders, J. S., Fabian, A. C., et al. 2010, MNRAS, 406, 1721
Ryu, D., Kang, H., Cho, J., & Das, S. 2008, Science, 320, 909
Santos, J. S., Tozzi, P., Rosati, P., & Böhringer, H. 2010, A&A, 521, 64
Sarazin, C. L. 1988, X-ray Emission from Clusters of Galaxies (Cambridge: Cambridge Univ. Press)
Simionescu, A., Allen, S. W., Mantz, A., et al. 2011, Science, 331, 1576
Snowden, S. L., Mushotzky, R. F., Kuntz, K. D., & Davis, D. S. 2008, A&A, 478, 615
Sunyaev, R. A., & Zeldovich, Ya. B. 1972, A&A, 20, 189
Tozzi, P., & Norman, C. 2001, ApJ, 546, 63
Tucker, W., Tananbaum, H., & Fabian, A. 2007, Sci. Am., 296, 42
Urban, O., Werner, N., Simionescu, A., Allen, S. W., & Bhringer, H. 2011, MNRAS, 414, 2101
Voit, G. M. 2005, Rev. Mod. Phys., 77, 207
Voit, G. M., & Donahue, M. 2005, ApJ, 634, 955
Wang, J., Navarro, J. F., Frenk, C. S., et al. 2011, MNRAS, 413, 1373
Wechsler, R. H., Zentner, A. R., Bullock, J. S., Kravtsov, A. V., & Allgood, B. 2006, ApJ, 652, 71
Wik, D. R., Sarazin, C. L., Finoguenov, A., et al. 2009, ApJ, 696, 1700
Wong, K.-W., & Sarazin, C. L. 2009, ApJ, 707, 1141
Yoshikawa, K., & Suto, Y. 1999, ApJ, 513, 549
Zhao, D. H., Mo, H. J., Jing, Y. P., & Börner, G. 2003, MNRAS, 339, 12